Study of the influence of turbulent flows on the aerodynamic performance of fixed-wing aircraft type UAV MALE

Catalin CUCU*,[1], Cristina PUPAZA[2], Bart JANSSENS[3], Mihai MIHAILA-ANDRES[4]

*Corresponding author
[1]Technological Development Center, Military Technical Academy "Ferdinand I", B-dul George Cosbuc 39-49, Bucharest 050141, Romania, ionut.cucu@mta.ro*
[2]Department of Robots and Manufacturing Systems, POLITEHNICA University of Bucharest, Splaiul Independentei 313, 060032, Bucharest, Romania, cristinapupaza@yahoo.co.uk
[3]Department of Mechanical Engineering, Royal Military Academy of Belgium, Renaissance avenue 30, 1000 Brussels, Belgium, bart.janssens@mil.be
[4]Department of Aircraft Integrated Systems and Mechanics, Military Technical Academy "Ferdinand I", B-dul George Cosbuc 39-49, Bucharest 050141, Romania, mihai.mihaila@mta.ro

DOI: 10.13111/2066-8201.2023.15.4.9

Received: 23 October 2023/ Accepted: 13 November 2023/ Published: December 2023

Abstract: *A study of the air behavior in the near-wake region of the NACA0012 airfoil infinite wing model at low Reynolds numbers was conducted. The study consisted of comparing the results obtained from experiments with those from numerical simulations. The numerical results of the velocity profiles in the near-wake region showed good agreement with those provided by the PIV system for most of the simulations and those in the literature. In addition, boundary layer separation and reattachment forming a laminar separation bubble along the airfoil was captured using simulations in Ansys Fluent and compared with a literature database to better confirm the simulation results. The UAVs have a complex cross-section shape of the fuselage. The second part of this paper explores the aerodynamic consequences of its shape, at the operational flight ceiling, in a comparative approach for three different fuselage designs.*

Key Words: *low Reynolds numbers, LES, PIV, near-wake, laminar separation bubble, Spalart-Allmaras, UAV fuselage*

1. INTRODUCTION

Nowadays the unmanned aerial vehicles are employed on a large scale, from military to industry implementations, from battlefields to smaller units that people may be play outdoor.

The military industry drones recorded an exponentially growth worldwide since ’90s. They are used in missions that are dangerous for humans and can stay in the air for a large period of time. Under these circumstances, one of the most important advantages of the UAVs is their ability to remote control, which has made them popular in the aviation industry and especially in the military industry. The design of UAVs requires special attention due to the fact that the evolution in flight and its control is done remotely. Thus, great efforts are done on the structural design of these vehicles and in particular in their aerodynamic design. Simulating the air flow around the UAV is of great importance for studying the aerodynamic forces and stability of the aircraft during flight in order to determine optimal models to suit the missions they have to accomplish. The use of the Finite Element Method (FEM) software such as ANSYS Fluent can significantly reduce the costs of the design, construction and testing of these complex structures.

2. LOW REYNOLDS NUMBERS TURBULENT FLOWS

The formation and burst of a laminar separation bubble (LSB) has long been known to induce a negative effect to the performance of airfoils operating at low Reynolds number regime ($Re < 10^5$). Compared to the essentially turbulent flows that are encountered at high Reynolds numbers, laminar flows have a significantly greater propensity to experience detrimental separation. In the presence of an adverse pressure gradient, a laminar boundary layer can separate and reattach, thus forming a LSB.

The problem considered here is that of investigating the near-wake region velocity profiles of a NACA0012 at angles of attack of 3° and 6° for Reynolds numbers of 25 000, and 49 000. This airfoil was selected due to the availability of very precise experimental data in the literature. Kim et al. [1] visualized the laminar separation bubble and transition on a NACA0012 airfoil according to angle-of-attack by using a smoke-wire visualization technique with similar low Reynolds numbers. They suggested that the separation bubble and transition are three-dimensional phenomena.

Finite element method using Large Eddy Simulation (LES) was carried out with a commercial flow solver, Ansys Fluent 2021R2 [2], for comparison with experimental data for the velocity profiles in the near-weak region of the airfoil. In addition, the laminar separation, transition, and subsequent three dimensional breakdown were captured in the Ansys Fluent simulation. In view of the growing interest in low-pressure turbines, micro air vehicles (MAVs), and unmanned aerial vehicles (UAVs) that have small weights and sizes, a deeper understanding of LSB-related phenomena and to its consequences in the near-wake are necessary.

2.1 Experimental set-up and procedure

An optical, non-intrusive method that is related to both, flow visualization and optical point techniques, has developed over the last 20 years called Particle Image Velocimetry (PIV). This technique can provide a quantitative measure including its uncertainty of the instantaneous flow velocity field across a planar area of a flow field. PIV has become an important tool for quantitative and instantaneous measurements of laboratory flows. The flow is seeded with tiny, neutrally buoyant particles – so-called ’tracers’– e.g. oil or water aerosols in air and solid particles in fluids or flames. Recently, also Helium-filled soap bubbles have been introduced for air flow measurements. Their diameter ensures a largely more intense light scattering behavior. Using a light sheet, formed by passing a double pulsed laser beam through an optical arrangement including cylindrical lenses, the particles in the flow are illuminated twice with a

small time separation [3]. The particle positions at both instants of time of the laser pulses are recorded. The recorded particle displacement field is measured locally across the whole field of view of the images, scaled by the image magnification and then divided by the known pulse separation to obtain flow velocity at each point. A camera positioned typically perpendicular to the plane of the light sheet is shuttered to capture the light scattered from the particles. Depending on the flow velocity and the factor of magnification of the camera lens the delay of the two pulses have to be chosen such that adequate displacements of the particle images on the CCD are obtained. From the time delay between the two illuminations and the displacement of the tracers, velocity vectors can be calculated.[3]

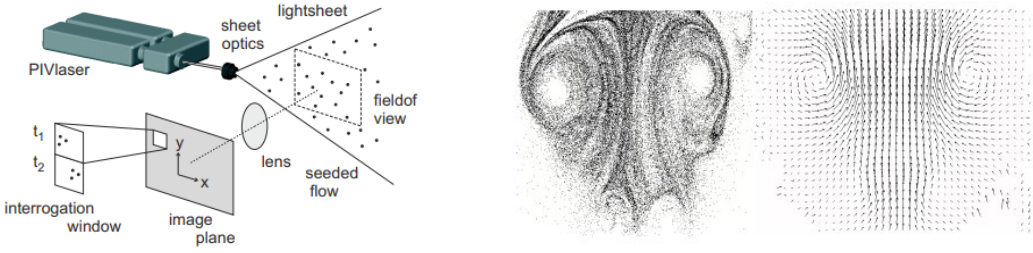

Figure 1: General setup of 2D PIV system (left); Seeded vortex and corresponding flow field (right)[3]

For the evaluation of the particle images, it is assumed that the tracers follow the flow at the local flow velocity between the two illuminations. The (digital) PIV recording is divided in small subareas – so-called 'interrogation windows'. Using statistical correlation techniques one local displacement vector is determined for each interrogation window. For this reason the size of this interrogation window is selected such that all particles within this area have moved homogeneously in the same direction and the same distance. For good results the number of particles within one interrogation window should be at least ten, and move no more than one quarter of the interrogation window size between the two recorded frames [3].

In order to carry out the experiments, a NACA 0012 wing profile with a chord length of 120 mm was 3D printed with resin to ensure a smooth surface for the wing profile. The objective being to measure the properties of the fluid in the wake of the wing profile. The experimental set-up is shown in the photo below.

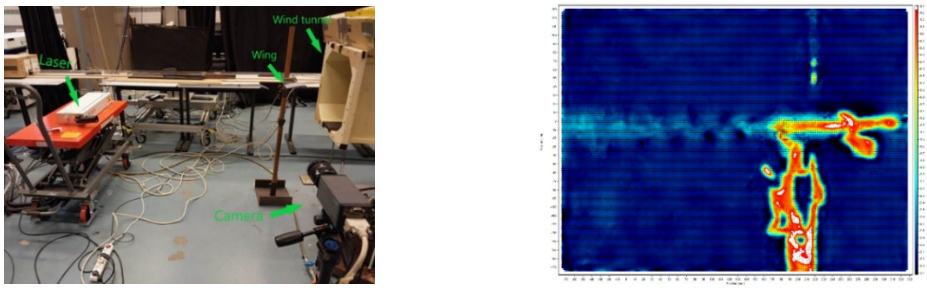

Figure 2: Experimental set-up used (left); Post-processing PIV result (right)

Four experiments were performed. Two, with a 3° angle of attack and Reynolds numbers of 25000 and 49000. And two more, with a 6° angle of attack and the same Reynolds numbers. For post-processing of PIV results it was used the LaVision [3] software. At this step it was observed that the metal bar which was used to fix the wing profile at a certain angle of attack reflected a part of the laser light, so that measurement errors occurred just near the trailing edge of the wing. This is illustrated in the right side of the figure above which shows the velocity measurement for an angle of attack of 3° and a Reynolds number of 25000.

2.2 Computational methodology

The motion of a compressible Newtonian fluid is governed by the Navier-Stokes (N-S) equations, which express the conservation of mass, momentum, and energy:

$$\frac{\delta\rho}{\delta t}+\frac{\delta}{\delta x_i}(\rho u_i)=0, \tag{1}$$

$$\frac{\delta}{\delta t}(\rho u_i)+\frac{\delta}{\delta x_j}\left(\rho u_i u_j\right)=-\frac{\delta p}{\delta x_i}+\frac{\delta \tau_{ij}}{\delta x_j}, for\ i\in\{1,2,3\}, \tag{2}$$

$$\frac{\delta}{\delta t}(\rho E)+\frac{\delta}{\delta x_j}\left[u_j(\rho E+p)\right]=-\frac{\delta q_j}{\delta x_j}+\frac{\delta}{\delta x_j}(u_i\tau_{ij}), \tag{3}$$

where the viscous stress tensor, τ_{ij}, and the heat flux, q_j, are given by, respectively,

$$\tau_{ij}\equiv\mu\left[\left(\frac{\delta u_i}{\delta x_j}+\frac{\delta u_j}{\delta x_i}\right)-\frac{2}{3}\frac{\delta u_k}{\delta x_k}\delta_{ij}\right], \tag{4}$$

$$q_j\equiv\frac{\mu}{Pr}\frac{\delta}{\delta x_j}\left(\rho u_i u_j\right)=\left(E+\frac{p}{\rho}-\frac{1}{2}u_k u_k\right), \tag{5}$$

In the above equations, ρ denotes the fluid density, u_i the velocity component in the direction x_i, p the static pressure, E the total energy per unit mass, μ the dynamic viscosity coefficient, and Pr the flow Prandtl number assumed to be constant. The system is closed with the *ideal gas* equation of state written in the form:

$$p=(\gamma-1)\rho\left(E-\frac{1}{2}u_k u_k\right), \tag{6}$$

For all the flows considered in the present work, the specific heat ratio is set to $\gamma=1.4$ and the Prandtl number to $Pr=0.85$. Moreover, for the dynamic viscosity a *Sutherland's law* is assumed for more precise results even if only low Mach number flows are considered:

$$\mu=\frac{1}{Re}\left(\frac{T}{T_\infty}\right)^{3/2}\frac{T_\infty+T_S}{T+T_S}, \tag{7}$$

in which T_S is 110.3K.

An advanced sub-grid-scale (SGS) model developed by Nicoud and Ducros [4], named Wall-Adapting Local Eddy (WALE), that takes into account the strain and rotation rates of the smallest resolved turbulent fluctuations was chosen for the LES simulations. For this particular model the eddy viscosity is expressed by:

$$\nu_T=(C_W\Delta)^2\frac{\overline{OP_1}}{\overline{OP_2}+\varepsilon}=(C_W\Delta)^2|\overline{N_{ij}}|, \tag{8}$$

where C_W is the WALE constant model, Δ is the characteristic length scale representing the cell size, and $\varepsilon=10^{-6}$. Besides, the other participating quantities are:

$$\overline{OP_1}=\left(S_{ij}^d S_{ij}^d\right)^{3/2}, \overline{OP_2}=\left(\overline{S_{ij}S_{ij}}\right)^{5/2}+\left(S_{ij}^d S_{ij}^d\right)^{5/4} \tag{9}$$

in which

$$S_{ij}^d=\frac{1}{2}\left(\overline{g_{ij}^2}+\overline{g_{ji}^2}\right)-\frac{1}{3}\sigma_{ij}\overline{g_{kk}^2}, \overline{g_{ij}}=\frac{\delta\overline{u_i}}{\delta x_j} \tag{10}$$

2.3 Computational domain and grids

The steps followed for making the mesh for 2D fluid flow domain for Ansys Fluent are:

- 2D airfoil points with an unit of chord length c are imported into Catia V5R18 [5] and a surface is generated.
- This model is imported in Ansys DesignModeler and a C-type domain is generated around of it. The axes are set up with x being the chord-wise direction and z the span-wise direction, such that the leading-edge is located along the line x=0, y=0.
- From the wing's leading-edge line, the domain extends 15 chord lengths upstream, 20 chord lengths downstream, 15 chord lengths above, and 15 chord lengths below to avoid confinement effects. Thus, if we denote by c the chord length, the domain has the range $[-15c,20c]\times[-15c,15c]$ along the chord-wise, and vertical directions, respectively.
- The domain is divided in several parts to obtain a structured mesh. A horizontal line on the middle of the airfoil from inlet to outlet, a vertical line at the trailing edge and a vertical line at 10% c of the airfoil.
- This model is then imported into the general mesh module from Ansys package for meshing. A fix number of elements with a byas factor method is used so that the zones closer to the airfoil has high grid density and in the outer zone the mesh density is gradually increased. The mesh is coarsened as it goes outward away from the surface of the airfoil. For vertical lines and the horizontal one upstream, the value of 400 elements and a byas factor of 500,000 is chosen. For horizontal lines downstream, the value of 300 elements and a byas factor of 600 is chosen. For the upper and lower parts after 10% c of the airfoil the value of 1,200 elements and for the leading edge the value of 159 elements are chosen. A quadcore mesh is generated and 1,34 million nodes domain is obtained.

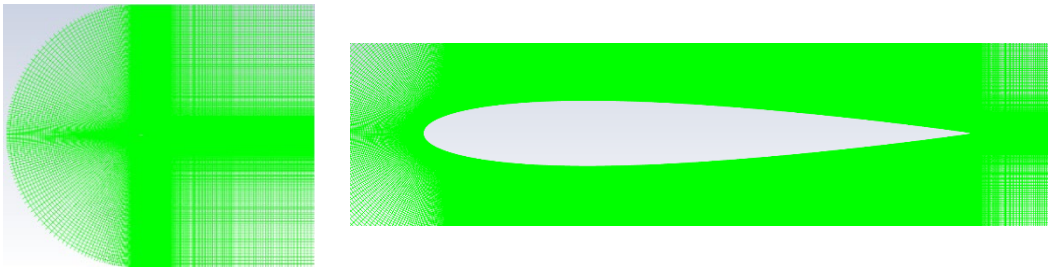

Figure 3: Span-wise plane of the 2D grid: domain (left), closer view on airfoil (right)

The steps followed for making the mesh for 3D fluid flow domain for Ansys Fluent are:

- 2D airfoil points with an unit of chord length c, the specific angle of attack are imported into Catia V5R18 and an extruded part of c/30 is generated for each.
- These parts are imported in Ansys DesignModeler and C-type domains are generated around of them. The axes are set up with x being the chord-wise direction and z the span-wise direction, such that the leading-edge is located along the line x =0, y =0.
- From the wing's leading-edge line, the domain extends 10 chord lengths upstream, 15 chord lengths downstream, 10 chord lengths above, and 10 chord lengths below to avoid confinement effects. Thus, if we denote by c the chord length, the domain has the range $[-10c,15c]\times[-10c,10c]\times[0,c/30]$ along the chord-wise, vertical, and span-wise directions.
- This model was then imported into the ICEM-CFD [6] module available in Ansys package for meshing. A blocking approach with O-grid is used to discretize the domain into various zones. The zones closer to the airfoil has high grid density, obtained by enclosing two layers of very fine mesh with 41, respectively 25 points. The airfoil is divided in two parts at 10%

c. The upper and lower parts after 10% c of the airfoil the value of 400 points and for the leading edge the value of 100 points are chosen. The near-weak region is obtained by dividing the domain with two vertical lines, one on trailing edge and one at 1.5 c distance, with the value of 100 points. In the outer zone the mesh density is gradually increased, thus the mesh is coarsened as it goes outward away from the surface of the airfoil and a value of 25 points is chosen. In span-wise direction the value of 31 points is chosen. For each case was calculated the wall Y+, in relation with air velocity, compose of 40 inflation layers and the estimated distance is fixed at Y+ <= 1. A hexcore mesh is generated and 3,3 million nodes domain is obtained for each case with the quality of the mesh between 0.8 and 1 reported by the ICEM-CFD.

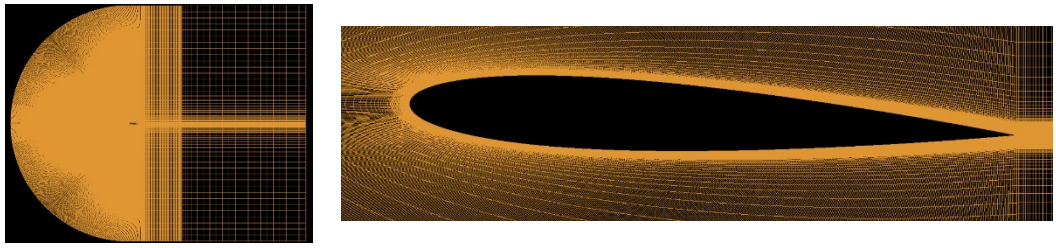

Figure 4: Span-wise plane of the 3D grid: domain (left), closer view on airfoil (right)

2.4 Initial and Boundary conditions

For Ansys Fluent, the initial and boundary conditions were specified in the following manner:

- A pressure-based solver with double precision, gravitational acceleration and Equation of Energy ON is chosen.
- The gas considered (in the simulations) is air at the atmospheric conditions of the sea level and ideal-gas model is chosen for density and Sutherland's low for dynamic viscosity.
- The Inlet is considered as velocity-inlet with the value of the velocity magnitude in respect with the value of Reynolds numbers of 25 000, and 49 000 respectively, and the Outlet is considered as pressure-outlet.
- A coupled solution scheme with Rhie-Chow distance based flux type is chosen and the simulations were initialized as hybrid.

The calculations were carried on for 3000 iterations with a value of 0.001 s of the time step and 10 iterations/time step.

After the first 2000 iterations the flow behavior is stable and data sampling for time statistics is activated for the last 1000 iterations to capture the time-average values of the velocity.

2.5 Laminar separation bubbles results

Computed time average velocity magnitude and stream lines can be seen in the Figure 5 and 7. Also, the instantaneous iso-surfaces of Q-criterion are shown for better visualisation of the vortices in 3D.

The results of the 2D simulation are fitted alongside those of the 3D simulation in order to make a first comparison.

The black arrows represent the separation and reattachment points of the Laminar Separation Bubbles (LSB).

Re 2.5x10^4 Re 4.9x10^4

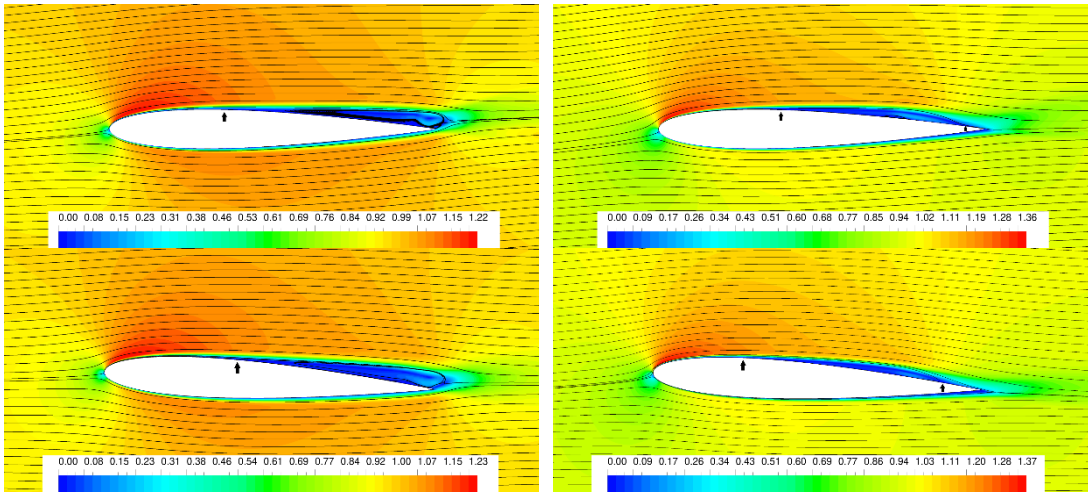

Figure 5: Average velocity magnitude and stream lines at 3° (2D grid above & 3D grid below)

Re 2.5x10^4 Re 4.9x10^4

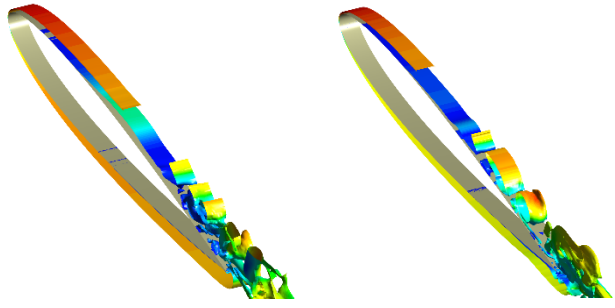

Figure 6: Instantaneous ISO-Surface Q criterion 3°

Re 2.5x10^4 Re 4.9x10^4

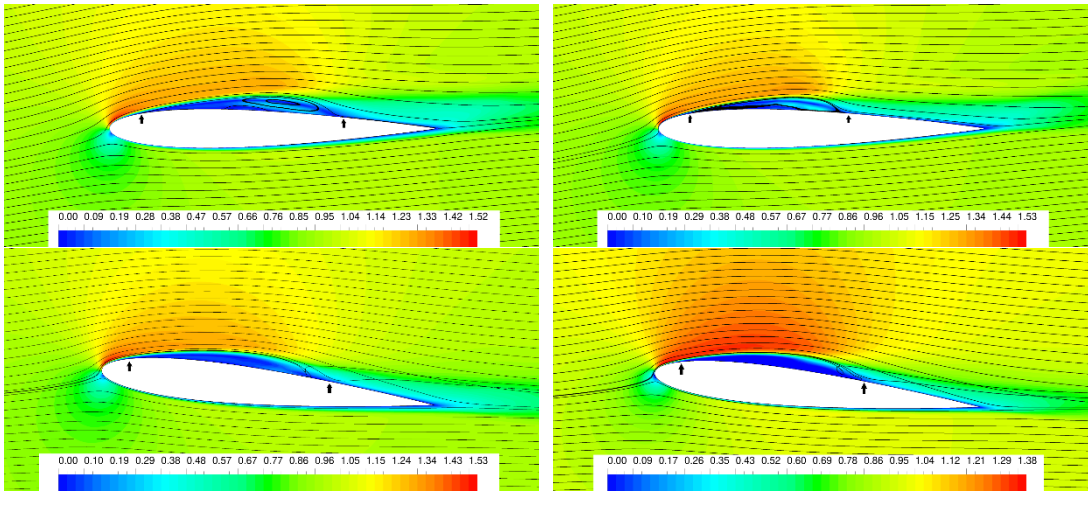

Figure 7: Average velocity magnitude and stream lines at 6° (2D grid above & 3D grid below)

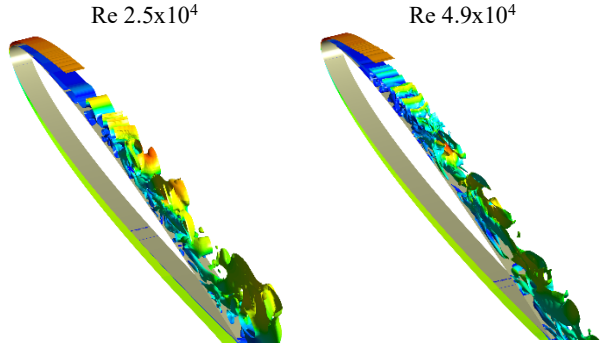

Figure 8: Instantaneous ISO-Surface Q criterion 6°

It is clearly visible that the results are relatively similar. However, the height of the bubble from the 2D simulation looks to be higher compared to the one from the 3D simulation. This can be explained by the fact that at these Reynolds numbers the flow is three-dimensional and contains structures that vary in the span-wise direction. This can be seen in the instantaneous iso-surfaces of Q-criterion in Figure 6 and Figure 8. The iso-surfaces are not cylindrical and reveal significant span-wise variations. In order to better verify the true behavior of our detachment bubbles, comparisons with results found in the literature are better supported in the table below.

Table 1: LSB Separation and Reattachment points

Source	$\alpha°$	Re	Separation x_s/c	Reattachment x_r/c	Bubble length
Kim [1]	3	$2.3x10^4$	0.506	-	0.494c
2D		$2.5x10^4$	0.444	-	0.556c
3D		$2.5x10^4$	0.444	-	0.556c
Kim [1]	3	$4.8x10^4$	0.417	-	0.583c
2D		$4.9x10^4$	0.389	0.928	0.539c
3D		$4.9x10^4$	0.278	0.889	0.611c
Kim [1]	6	$2.3x10^4$	0.256	0.812	0.556c
2D		$2.5x10^4$	0.139	0.694	0.555c
3D		$2.5x10^4$	0.111	0.694	0.583c
Kim [1]	6	$4.8x10^4$	0.143	0.644	0.501c
2D		$4.9x10^4$	0.111	0.567	0.456c
3D		$4.9x10^4$	0.111	0.639	0.528c

In the Table 1 here above, comparisons between measurements of the separation and reattachment points from the experimental data of the Kim et al. [1] article and the Ansys Fluent 2D and 3D simulations are summarized.

- In the case of 3° Re=$2.3x10^4$ there is a difference of 12% for the separation point and a 12% for the bubble length along the chord. In the study of Kim et al. [1] there is no reattachment point.
- In the case of 3° Re=$4.8x10^4$ there is a difference of 7% for 2D grid and a 33% for 3D grid for the separation point. Also in this case there is no experimental data for the reattachment point. And for the bubble length along the chord there is a difference of 7.5%, and 5% respectively.
- In the case of 6° Re=$2.3x10^4$ there is a difference of 46% and 57% for the separation point and a 14.5% for the reattachment point. The differences for the bubble length along the chord are of a magnitude of 0.2%, and 5% respectively.

- For the last case of 6° Re=4.8x10^4 there is a difference of 22% for the separation point and for the reattachment point 12%, and 0.8% respectively. For the bubble length along the chord there is a difference of 9%, and 5.5% respectively.

It can be said that the model is acceptable for modelling LSBs. In view of all the simplifying assumptions used in the numerical simulation models, it goes without saying that it is reliable for approximate results. To improve the results, an increase of the mesh resolution in the boundary layer of the airfoil can be increased.

2.6 Near-wake velocity profiles

Figure 9 shows the time average velocity profiles in the near-weak region obtained with the PIV system, Ansys Fluent and the experimental results from literature. As already mentioned in the experimental part presented above, measurement errors are very large in the part just behind the trailing edge. This has led us not to retain the measurements in this area and to focus only on the measurements from 30% of the chord length from the trailing edge. Thus, measurements were made at x/c=0.3, 0.5 and 1.0.

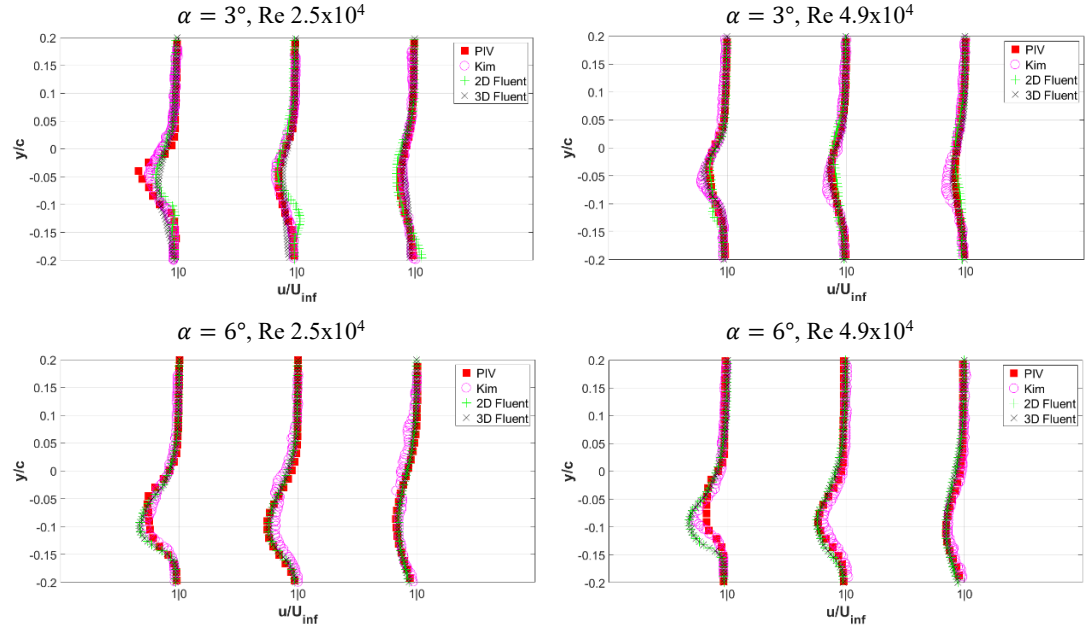

Figure 9: Average velocity magnitude profiles of near-wake

Possible errors that could influence the results are the following:

- Errors due to the experimental measurement tools, especially PIV. But the largest error issue has been ruled out due to background noise near the trailing edge. Thus, given the known level of precision of the PIV, we assume that the errors of the experimental measurements remain quite negligible.
- Secondly, simulation errors are the most likely to occur because they are based on a theoretical model which itself has approximations of reality. Also, the computational capabilities to fully meet the satisfactions of the theoretical model are quite limited. Therefore, it goes without saying that the errors are mainly to be found in the numerical simulations.

The 3D simulation and the experimental results agree quite well despite the disadvantages that a numerical simulation can have. Nevertheless, the 2D simulation doesn't have as good results

as the 3D simulation, especially in the case of the 3° angle of attack. This could be explained by the fact that two-dimensional turbulence has different physical behavior than three-dimensional turbulence and it will capture the fluid behavior less well.

3. AERODYNAMIC ANALYSIS OF THE FUSELAGE OF A FIXED WING AIRCRAFT TYPE UAV MALE

The aerodynamic configuration of a transport aircraft's fuselage plays a pivotal role in the preliminary design. Approximately 30% of the total zero lift drag can be attributed to the fuselage. Key aspects of aircraft cruise performance, such as maximum flight speed and fuel efficiency, are primarily influenced by the zero lift drag coefficient, and these factors can be significantly enhanced through more precise aerodynamic fuselage design. Additionally, the longitudinal and directional stability characteristics of an aircraft are intimately connected to the fuselage's contribution. Therefore, an accurate assessment of the latter could lead to better aircraft design and improved aircraft stability characteristics. [7], [8]

3.1 Presentation of models

Following a preliminary study conducted on a sample of twenty aircrafts, three reference aircrafts were chosen, the CAD models were generated in order to be analyzed in Ansys Fluent software from the aerodynamic point of view.

The three CAD models presented below are similar, having the same wing, V empennage, surveillance devices, propellers, intake device and exhaust device, the difference being the shape and cross-sectional area of the fuselage so that the analysis is conducted under the same conditions and the results obtained can be compared strictly from this point of view.

Geometric features of the models:

- The length of the fuselage is about 8.5 m for the three models;
- The wingspan is 17.3 m;
- The half-wingspan of the empennage V is 1.2 m;
- The diameter of the propeller is 3 m;
- The average diameter of the cross-sections of the fuselage is 0.84 m, 0.61 m, and 0.92 m.

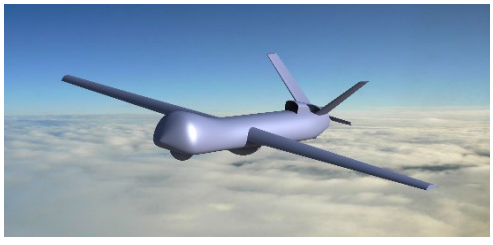

Figure 10: Model 1 [9]

Figure 11: Elbit Hermes 900 [10]

Figure 12: Model 2 [9]

Figure 13: Orion UAV [11]

Figure 14: Model 3 [9]

Figure 15: MQ-4 Triton [11]

3.2 Description of the cross-section shape of the models

To achieve the cross-section shape of the models, a super-ellipse function was implemented in the MATLAB software:

$$Y = C \cdot Z^{N_1} \cdot (1 - Z)^{N_2}, \tag{11}$$

where
$Z = [0,1]$,
N_1 is a coefficient for the curvature of the lower part,
N_2 is a coefficient for the curvature of the upper part,
C is a scaling coefficient.

The CAD model was created in CATIA V5 software by importing 400 points, which were calculated in MATLAB software, in the characteristic sections of the model aircrafts (Fig. 14, Fig. 15, Fig. 16).

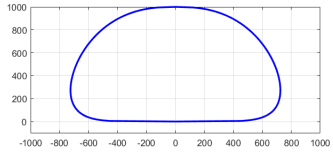

Figure 16: Model 1: Shape of the cross-section in MATLAB [9]

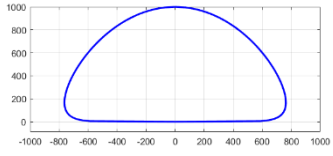

Figure 17: Model 2: Shape of the cross-section in MATLAB [9]

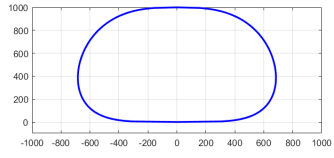

Figure 18: Model 3: Shape of the cross-section in MATLAB [9]

3.3 Computational domain and grids

The fluid flow domain is C-type being designed around a half of the models and has a structured poly-hexcore mesh, which was generated in ANSYS Fluent with meshing 2021 R1.

The eight layers around the aircraft components are uniform and have been computed so that the first layer and growth ratio are specific to them for the most accurate turbulence results close to the walls.

All three domains have approximately 3.5 million elements, and the domain boundaries have been set so that confinement effects are avoided.

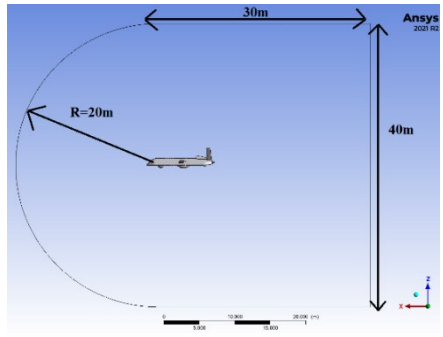

Figure 19: Domain dimensions [9]

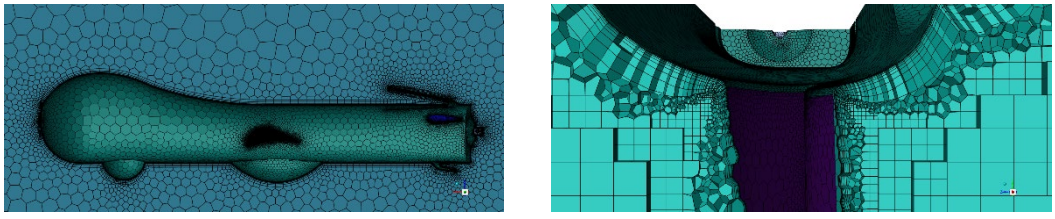

Figure 20: Span-wise view of the mesh (left); Cross-section view of the mesh (right) [9]

3.4 Computational methodology

In Reynolds-Averaged Navier-Stokes (RANS) models the N-S equations are divided into the average component and the fluctuation component. The total velocity u_i is defined as a function of the average velocity $\overline{u_i}$ and the fluctuating velocity u_i' as represented in the following equation:

$$u_i = \overline{u_i} + u_i', \tag{12}$$

The continuity and momentum equations incorporating these instantaneous flow variables are given by:

$$\frac{\delta \rho}{\delta t} + \frac{\delta}{\delta x_i}(\rho u_i) = 0, \tag{13}$$

$$\frac{\delta}{\delta t}(\rho u_i) + \frac{\delta}{\delta x_i}(\rho u_i u_j) = \frac{\delta \rho}{\delta x_i} + \frac{\delta}{\delta x_j}\left[\mu\left(\frac{\delta u_i}{\delta x_j} + \frac{\delta u_j}{\delta x_i}\right) - \frac{2}{3}\frac{\delta u_i}{\delta x_i}\delta_{ij}\right] + \frac{\delta}{\delta x_i}(-\rho\overline{u_i' u_j'}), \tag{14}$$

These equations (in Cartesian form of tensor) are known as RANS, and the term $-\rho\overline{u_i' u_j'}$ must be modeled. The Boussinesq hypothesis is applied in relation to the Reynolds stresses and the average velocity:

$$-\rho\overline{u_i' u_j'} = \mu_t\left(\frac{\delta u_i}{\delta x_j} + \frac{\delta u_j}{\delta x_i}\right) - \frac{2}{3}\left(\rho k + \mu_t \frac{\delta u_k}{\delta x_k}\right)\delta_{ij}, \tag{15}$$

The modified continuity equation for this turbulence model solves the turbulent viscosity term ν:

$$\frac{\delta}{\delta t}(\rho\tilde{\nu}) + \frac{\delta}{\delta x_i}(\rho\tilde{\nu}u_i) = G_\nu = \frac{1}{\sigma\tilde{\nu}}\left[\frac{\delta}{\delta x_j}(\mu + \rho\tilde{\nu})\frac{\delta\tilde{\nu}}{\delta x_j} + C_{b2\rho}\left(\frac{\delta\tilde{\nu}}{\delta x_j}\right)^2\right] - Y_\nu + S\tilde{\nu}, \tag{16}$$

where G_ν represents the production of turbulent viscosity and Y_ν represents the destruction of turbulent viscosity. Turbulent viscosity is calculated as follows:

$$\mu_t = \rho\tilde{\nu} f_{\nu 1}, \tag{17}$$

$f_{\nu 1}$ is the viscous damping function:

$$f_{\nu 1} = \frac{\lambda^3}{\lambda^3 + C_{\nu 1}^3}. \tag{18}$$

3.5 Initial and Boundary conditions

For Ansys Fluent, the initial and boundary conditions were specified in the following manner:

- A pressure-based solver with double precision and gravitational acceleration is chosen.
- The gas considered (in the simulations) is air at the atmospheric conditions of the flight ceiling of 10,000 m, density and dynamic viscosity being constant.
- The Inlet is considered as velocity-inlet with the value of the velocity magnitude of 60m/s and an angle of attack of 5°, corresponding to a Mach number of 0.2 and a Reynolds number of 1,344,000, and the Outlet is considered as pressure-outlet.
- A coupled solution scheme with Rhie-Chow distance based flux type is chosen and the simulations were initialized as hybrid.

The calculations were performed for only 500 iterations because the analysis of the aerodynamic coefficients set for the wing, empennage, fuselage, propeller and the whole assembly showed a stable value for the last 100 iterations.

3.6 Comparison of the results achieved for the three models

a) Static pressure distribution

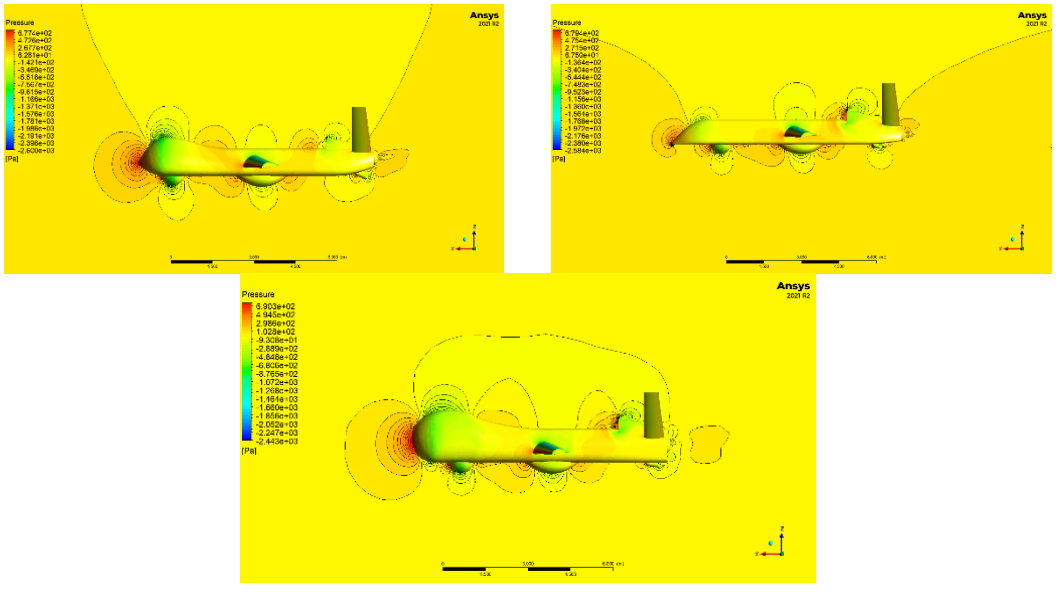

Figure 21: Detailed close view of static pressure around the fuselage models [9]

- The first model has the lowest value of the static pressure which can be transposed in the lowest drag force, because the leading edge of the fuselage is sharp.
- The third model has the higher value of the static pressure because the leading edge of the fuselage is robust.

- The second model has an intermediate value of the static pressure because of the engine's inlet, but it has the lowest value of the static pressure at the leading edge of the fuselage compared to the other two models.
- All three models create a relatively good distribution of the lift force on the upper surface.

From this point of view model one is better in this configuration because the shape of it disperses rapidly the drag force.

b) Velocity distribution

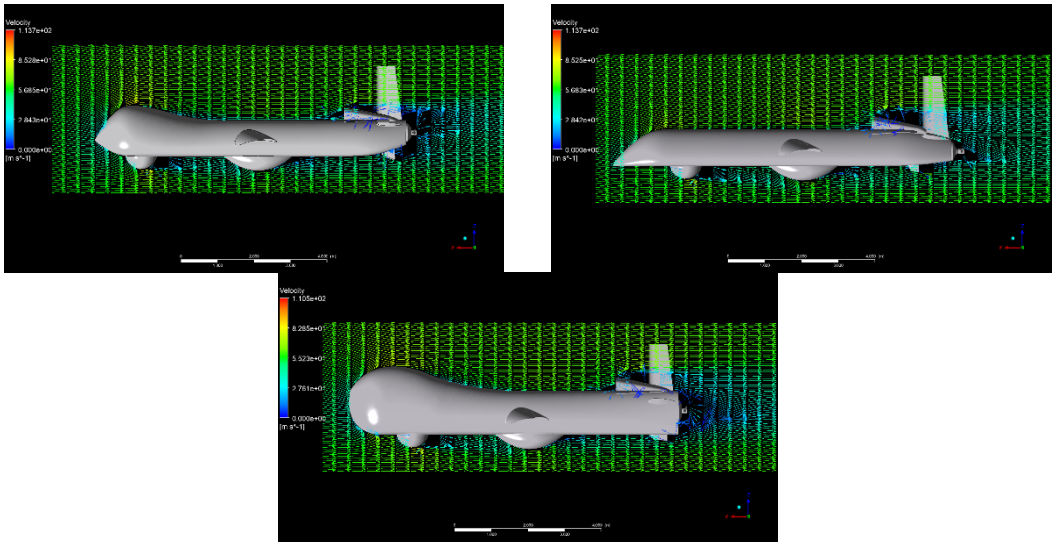

Figure 22: Vertical velocity distribution around the fuselage models [9]

- All three models have a uniform distribution of the velocity around the upper and lower surface.

c) Eddy viscosity distribution

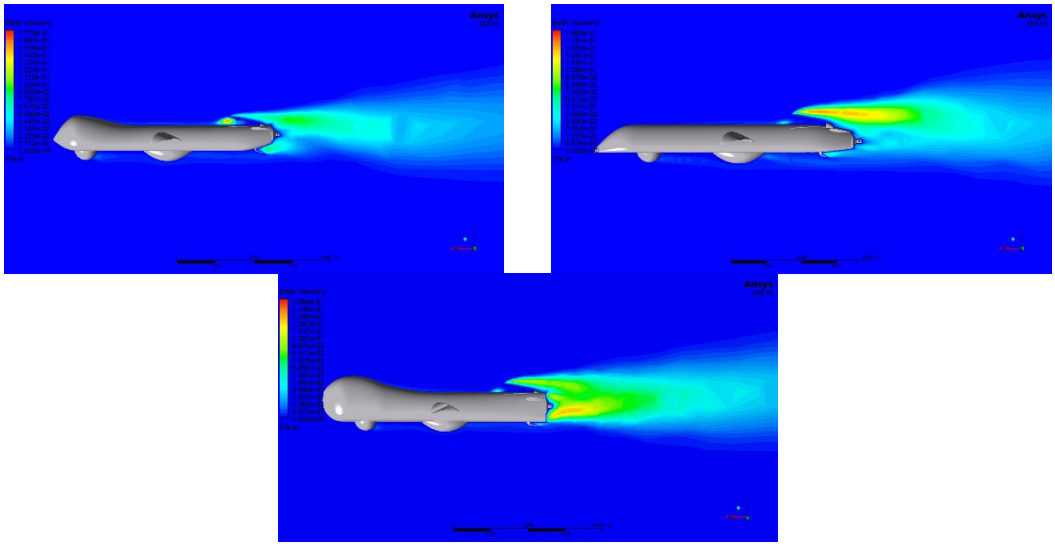

Figure 23: Close view of eddy viscosity around the fuselage models [9]

- All three models have a relatively low turbulence on the upper surface of the fuselage which can be transposed in a good design of this area.
- On the lower surface of the fuselage turbulence occur, because of the surveillance equipment.
- The third model shows the largest turbulence zone on the lower part of the trailing edge of the fuselage.
- All three models have a large area of turbulence behind the engine intake which cannot be avoided.
- The first model shows a higher value of turbulence at the air inlet to the engine intake device compared to the other two models, which may result in turbulent fluid flow in the engine.

From this point of view, Model 2 is better in this configuration because it has fewer areas that can create turbulence

4. FINAL CONCLUSIONS

Low Reynolds numbers turbulent flows:

- A comparative study between experimental and numerical measurements of velocity profiles in the near-field region following the NACA0012 wing profile for low Reynolds numbers was performed. Experimental measurements were performed using the PIV technique and simulations were performed in Ansys Fluent. From the results it can be stated that the model that gave the best results was LES with 3D discretization. It models the LSBs quite well and also gives results that agree very well with experimental and literature results.
- The results obtained for the boundary layer show similarities with those in the paper by Kim et al. [1], but there are significant errors between the separation and reattachment points. Errors that come from the relatively low resolution of the discretization used in the simulations and could be improved.

Aerodynamic analysis of the fuselage of a fixed wing aircraft type UAV MALE:

- The second model has the lowest drag force on the leading edge but also it has the lowest internal volume, which leads to poor equipment with surveillance devices.
- For models 1 and 3 at the front of the fuselage, a low-pressure zone is created due to the acceleration of the air fillets on the upper surface of the fuselage, which lead to the appearance of a positive momentum on the pitch axis.
- The third model has the largest turbulence zone at the trailing edge of the fuselage compared to the other two models, which can lead to a poor flow for the propeller and make it unstable.

REFERENCES

[1] Dong-Ha Kim et al., Boundary layer and near-wake measurements of NACA 0012 airfoil at low Reynolds numbers, In: *47th AIAA Aerospace Sciences Meeting Including the New Horizons Forum and Aerospace Exposition* 2009, p. 1472.
[2] * * * *ANSYS Fluent. ANSYS FLUENT, Release 2021R1, User's Guide*, 2021.
[3] * * * LaVision, *Product Manual: FlowMaster*, In: 2020.
[4] F. Nicoud and F. Ducros, Subgrid-scale stress modelling based on the square of the velocity gradient tensor. In: *Flow, Turbulence and Combustion* (Mar. 1999), pp. 183–200. doi: 10.1023/A:1009995426001.
[5] * * * *CATIA-Composites Design*, *CATIA V5R18* 2018.
[6] * * * ICEM Ansys, *ANSYS ICEM CFD Tutorial Manual*, 2015.
[7] F. Nicolosi et al., Fuselage aerodynamic drag prediction method by CFD, In: *5th CEAS Air Space Conference,* 2015.

[8] P. Della Vecchia and F. Nicolosi. Aerodynamic guidelines in the design and optimization of new regional turboprop aircraft, In: Aerospace Science and Technology **38** (2014), pp. 88–104. doi: 10.1016/j.ast.2014.07.018.

[9] C. Cucu and C. Pupăză, Aerodynamic analysis of the fuselage of a fixed wing aircraft type UAV using the finite element method. In: *Industrial engineering review- Faculty of Industrial Engineering and Robotics* (University POLITEHNICA of Bucharest), 2022.

[10] * * * *Swiss Select Hermes 900 as New UAS*, In: AIN online.com. url: https://www.ainonline.com/ aviation-news/defense/2014-06-11/swiss-select-hermes-900-new-uas.

[10] * * * *Russia announces Orion UAV sale to Middle East country*, In: Pakistan Defence. url: https: //pdf.defence.pk/threads/russia-announces-orion-uav-sale-to-middle-east-country. 574060/.

[11] * * * *MQ-4C Triton RQ-4 Global Hawk Thread*, In: Sino Defence Forum. url: https://www. sinodefenceforum.com/t/mq-4c-triton-rq-4-global-hawk-thread.7333/.